

## Article

# A Novel In Situ Sol-Gel Synthesis Method for PDMS Composites Reinforced with Silica Nanoparticles

Aldo Cordoba <sup>1</sup>, Juan Valerio Cauch-Rodríguez <sup>2</sup>, Rossana Faride Vargas-Coronado <sup>2</sup>,  
Rodrigo Velázquez-Castillo <sup>1</sup> and Karen Esquivel <sup>1,\*</sup>

<sup>1</sup> Graduate and Research Division, Engineering Faculty, Universidad Autónoma de Querétaro, Cerro de las Campanas, Queretaro 76010, Mexico; acordoba07@alumnos.uaq.mx (A.C.); rodrigo.velazquez@uaq.mx (R.V.-C.)

<sup>2</sup> Centro de Investigación Científica de Yucatán, Unidad de Materiales, C. 43 No. 130 x 32 y 34, Col. Chuburná de Hidalgo, Merida 97205, Mexico; jvcr@cicy.mx (J.V.C.-R.); ross@cicy.mx (R.F.V.-C.)

\* Correspondence: karen.esquivel@uaq.mx; Tel.: +52-442-192-1200 (ext. 65401)

**Abstract:** The addition of nanostructures to polymeric materials allows for a direct interaction between polymeric chains and nanometric structures, resulting in a synergistic process through the physical (electrostatic forces) and chemical properties (bond formation) of constituents for the modification of their properties and potential cutting-edge materials. This study explores a novel in situ synthesis method for PDMS-%SiO<sub>2</sub> nanoparticle composites with varying crosslinking degrees (PDMS:TEOS of 15:1, 10:1, and 5:1); particle concentrations (5%, 10%, and 15%); and sol-gel catalysts (acidic and alkaline). This investigation delves into the distinct physical and chemical properties of silicon nanoparticles synthesized under acidic (SiO<sub>2</sub>-a) and alkaline (SiO<sub>2</sub>-b) conditions. A characterization through Raman, FT-IR, and XPS analyses confirms particle size and agglomeration differences between both the SiO<sub>2</sub>-a and SiO<sub>2</sub>-b particles. Similar chemical environments, with TEOS and ethanol by-products, were detected for both systems. The results on polymer composites elucidate the successful incorporation of SiO<sub>2</sub> nanoparticles into the PDMS matrix without altering the PDMS's chemical structure. However, the presence of nanoparticles did affect the relative intensities of specific vibrational modes over composites from −35% to 24% (Raman) and from −14% to 59% (FT-IR). The XPS results validate the presence of Si, O, and C in all composites, with significant variations in atomic proportions (C/Si and O/Si) and Si and C component analyses through deconvolution techniques. This study demonstrates the successful in situ synthesis of PDMS-SiO<sub>2</sub> composites with tunable properties by controlling the sol-gel and crosslinking synthesis parameters. The findings provide valuable insights into the in situ synthesis methods of polymeric composite materials and their potential integration with polymer nanocomposite processing techniques.

**Keywords:** in situ synthesis; nanocomposites; sol-gel method; polymer coatings; reinforcers



**Citation:** Cordoba, A.; Cauch-Rodríguez, J.V.; Vargas-Coronado, R.F.; Velázquez-Castillo, R.; Esquivel, K. A Novel In Situ Sol-Gel Synthesis Method for PDMS Composites Reinforced with Silica Nanoparticles. *Polymers* **2024**, *16*, 1125. <https://doi.org/10.3390/polym16081125>

Academic Editors: Francisco Javier Espinach Orús and Quim Tarrés Farrés

Received: 23 March 2024

Revised: 10 April 2024

Accepted: 15 April 2024

Published: 17 April 2024



**Copyright:** © 2024 by the authors. Licensee MDPI, Basel, Switzerland. This article is an open access article distributed under the terms and conditions of the Creative Commons Attribution (CC BY) license (<https://creativecommons.org/licenses/by/4.0/>).

## 1. Introduction

Silicon polymers are widely used in various applications, owing to their being lightweight and flexible and their ease of sterilization, low cost, straightforward manufacturing processes, and remarkable resistance to physical aging and degradation. This extensive array of properties has enabled their application across virtually all industrial and research sectors [1]. Aligned with these attributes, the incorporation of nanoscale materials into polymeric materials has been the subject of extensive exploration in recent decades [2]. The incorporation of nanomaterials of diverse chemical (metals, ceramics, and polymers) and physical nature (nanoparticles, nanowires, nanoplates, etc.) has constituted a field of research in composite materials, being the nanocomposite polymers formed by the integration of nanostructured materials with a polymeric material as the matrix [3]. This investigation pursues a response to the continuous demand for materials with enhanced performance that the evolving industries require [4].

In recent years, numerous research efforts have focused on the design and evaluation of polymeric composites based on silicon polymers with nanostructures of varying morphologies and chemical nature [5]. This widespread investigation has been demonstrated in research that aimed to improve the physicochemical properties of polymeric materials by incorporating reinforcing nanostructures such as carbon nanotubes [6], metallic nanoparticles on polymeric fibers [7], and metal oxides [8] with an emphasis on applications in electronic and optical circuits. Other approaches seek to broaden the versatility of these polymeric matrices by imparting anticorrosive [9] or antimicrobial properties [10]. Similarly, the mechanical properties of different polymeric materials, including tensile strength, elastic modulus, and hardness [11,12], as well as barrier properties and separation membrane characteristics [13] have been modified through the use of nanostructured metal oxides.

Conventionally, two pathways are followed for obtaining these nanocomposite systems, an *ex situ* and *in situ* synthesis, each with thoroughly studied advantages and disadvantages [3]. In contrast to the *ex situ* method, the *in situ* composite synthesis has proven to be a potentially effective approach in addressing common challenges associated with the use of nanostructures, such as extensive synthesis times and limited polymer–reinforcement interactions often caused by agglomeration [14]. Among the most widely used synthesis methods, the sol-gel method stands out as the most extensively studied technique due to the easy integration of two synthesis methods and conditions for both materials [15].

The *in situ* formation of nanocomposite systems using substrates such as polydimethylsiloxane (PDMS) and metal oxide nanoparticles has presented significant advantages for the development of superhydrophobic surfaces [16], antimicrobial properties [17], fouling prevention [8], and insulating coatings [18]. The use of silica nanoparticles (SiO<sub>2</sub>) is particularly noteworthy in this context, where modifications in optical, mechanical, electrical, and chemical properties are achieved based on their size, surface chemistry, and porosity degree, which are adaptable during synthesis and under certain conditions [19].

Despite the advantages presented by *in situ* methods, a competition between polymerization reactions and particle synthesis, along with the presence of by-products formed in the chemical environment, sometimes proves incompatible, diminishing the formation of nanocomposite systems through this method [20].

In recent years, significant progress has been made in the development of *in situ* nanocomposites by utilizing polymeric materials as growth matrices for nanostructures, leading to the emergence of metal–polymer [21], polymer–polymer [22], and ceramic–polymer composite systems [23]. However, these advancements are hindered by the incomplete interaction between the polymer and nanostructures, resulting in surface composite materials rather than achieving full polymer–nanostructure integration. Despite the formation of composite systems, this superficial interaction restricts the final material properties to the surface level, failing to extend throughout the entire polymer matrix [24]. Furthermore, *in situ* nanocomposites such as Ag-Collagen [25] and ZnO-Chitosan [23] have been obtained through thermal processes to promote particle synthesis reactions and polymerization processes. However, this approach presents challenges in the composite fabrication methods, often requiring phase separation processes [21,22].

In response to these challenges, the versatility offered by the sol-gel method to modify the final properties of the material through synthesis conditions may present a potential solution for the development of *in situ* nanocomposites. By applying different synthesis conditions, a significant influence on the reactions occurring in polymer composite systems, such as hydrolysis, condensation, and crosslinking, has been observed [22].

Among these synthesis conditions, the hydrogen potential (pH) has proven to significantly alter the physicochemical properties of nanoparticles, as well as the hydrolysis and condensation reaction rates [15].

Therefore, the development of a methodology that mitigates the competition of chemical reactions during synthesis and facilitates integration between the polymeric and

nanoparticulate systems becomes an essential tool for overseeing the chemical processes occurring during nanocomposite manufacturing.

This research proposes a novel methodology for obtaining a polymeric nanocomposite with a PDMS matrix through the in situ synthesis of SiO<sub>2</sub> nanoparticles via the sol-gel method, utilizing pH as a control variable for initiating hydrolysis–condensation reactions and crosslinking processes with acidic and alkaline environments. This proposal aims to demonstrate a pathway that leverages the benefits of in situ synthesis to enhance the interaction and dispersion of nanostructured systems, as well as to reduce the competition of chemical reactions during the synthesis process.

## 2. Materials and Methods

Before the experimental procedures, all glassware utilized in the synthesis was thoroughly washed with ethanol, rinsed with distilled water, and dried with absorbent paper to eliminate potential impurities. The used reagents for the experimental procedures were dimethyl ketone (C<sub>3</sub>H<sub>6</sub>O) (99.5%, Meyer<sup>®</sup>, Mexico City, Mexico); hydroxy-terminated polydimethylsiloxane (PDMS-OH) (2550–3570 cSt, Sigma Aldrich<sup>®</sup>, Milwaukee, WI, USA); tetraethylorthosilicate (TEOS) (98% Sigma Aldrich<sup>®</sup>, Wuxi, China); ammonium hydroxide (NH<sub>4</sub>OH) (28% J.T.Baker<sup>®</sup>, Madrid, Spain); nitric acid (HNO<sub>3</sub>) (65–70% J.T.Baker<sup>®</sup>, Madrid, Spain); and dibutyltin dilaurate (DBTDL) (95% Sigma Aldrich<sup>®</sup>, Milwaukee, WI, USA).

### 2.1. SiO<sub>2</sub> Sol-Gel Synthesis

To ascertain the physicochemical characteristics of the components that constituted the polymeric composites, the synthesis of SiO<sub>2</sub> nanoparticles was conducted by employing the Stöber method [26,27] and a previously developed methodology in our research group [28,29] for both acidic and alkaline media.

Inside an inert environment (N<sub>2</sub>), acetone was stirred for 15 min. TEOS was added dropwise to the solution and mixed for 20 min. A weight ratio of 1:1.42 (C<sub>3</sub>H<sub>6</sub>O:TEOS) was used. For the alkaline SiO<sub>2</sub> synthesis, the hydrolysis reaction was initiated by adding ammonium hydroxide (NH<sub>4</sub>OH) dropwise as a catalyst until the pH reached 10 and by stirring for 2 h. The obtained gel was poured into a plastic petri dish and dried at room temperature for 24 h. For the synthesis under acidic conditions, a nitric acid (HNO<sub>3</sub>) catalyst was added dropwise until the pH reached 2. The stir and dry conditions for the acid synthesis were the same as those of the alkaline synthesis.

The synthesized particles were subjected to various characterization techniques. For morphological observation, TEM imaging was obtained using a JEM 2000FX transmission electron microscope, operating at 15 kV (JEOL USA; Peabody, MA, USA). XRD analyses were performed through a D8 Advance diffractometer (Bruker; Karlsruhe, Baden, Germany) with a Cu anode (20 kV, 20 mA, and  $\lambda = 1.5406 \text{ \AA}$ ). The scanned angular range was from 10 to 80 degrees in  $2\theta$  with a rate of 10° per minute. Raman spectroscopy was performed using a D2700M inVia Raman Microscope (Renishaw; Wetzlar, Hesse, Germany) equipped with an NdYHA laser with a wavelength of  $\lambda = 523 \text{ nm}$ . FT-IR analyses were performed with a Nicolet 8700 FT-IR spectrometer (Thermo Scientific; Madison, WI, USA) equipped with ATR equipment and operated under Absorbance mode. The XPS analysis was recorded using a K-Alpha Surface Analyzer (Thermo Scientific; Madison, WI, USA) equipped with a multichannel detector with X-ray 400  $\mu\text{m}$ -FG ON (400  $\mu\text{m}$ ).

### 2.2. Synthesis of PDMS/NP-SiO<sub>2</sub> Nanocomposites

The in situ synthesis of PDMS-%SiO<sub>2</sub> nanocomposites was carried out utilizing the sol-gel method and the crosslinking reaction of the hydroxyl-terminated PDMS matrix using magnetic and ultrasonic stirring techniques, as detailed in prior publications [28,29]. The synthesis initiates with a solution of acetone and the PDMS with a 1:0.6 weight ratio (PDMS: C<sub>3</sub>H<sub>6</sub>O). Mechanical stirring was applied to homogenize the solution for 1 h. TEOS was added according to the desired nanoparticle concentration (0%, 5%, 10%, and 15% by weight). The reported particle concentration values were derived from the weight

particle yields obtained during the SiO<sub>2</sub> sol-gel synthesis process and previous research [29]. Through this in situ synthesis, the concentration represented a categorical variable that denotes a relative number of particles incorporated within the composite.

To initiate the hydrolysis process and the formation of SiO<sub>2</sub> nanoparticles, the corresponding alkaline or acid catalyst (NH<sub>4</sub>OH or HNO<sub>3</sub>) was added dropwise until a pH of 10 (alkaline) or 2 (acidic) was achieved [27]. The solution was stirred for 2 h and then neutralized (pH 7). TEOS was added to the solution based on the desired matrix:crosslinker weight ratio (5:1, 10:1, and 15:1), and the mixture was stirred for 1 h. The solution was degassed by using an ultrasonic bath for 15 min to eliminate the remaining air bubbles. The solution was mechanically stirred for 5 min to reach room temperature.

The crosslinking reaction was initiated by adding the DBTDL catalyst dropwise with a weight ratio of 1:0.02 (PDMS:DBTDL). Finally, the solution was mechanically stirred for 5 min, deposited on an acrylic substrate, and left to cure at room temperature for 24 h.

Raman, FT-IR spectroscopy, and XPS analyses were conducted to identify chemical species with the same configurations used for SiO<sub>2</sub> NPs, such as characteristic vibrational modes. All of this was performed to determine the molecular composition of the synthesized composites.

### 3. Results

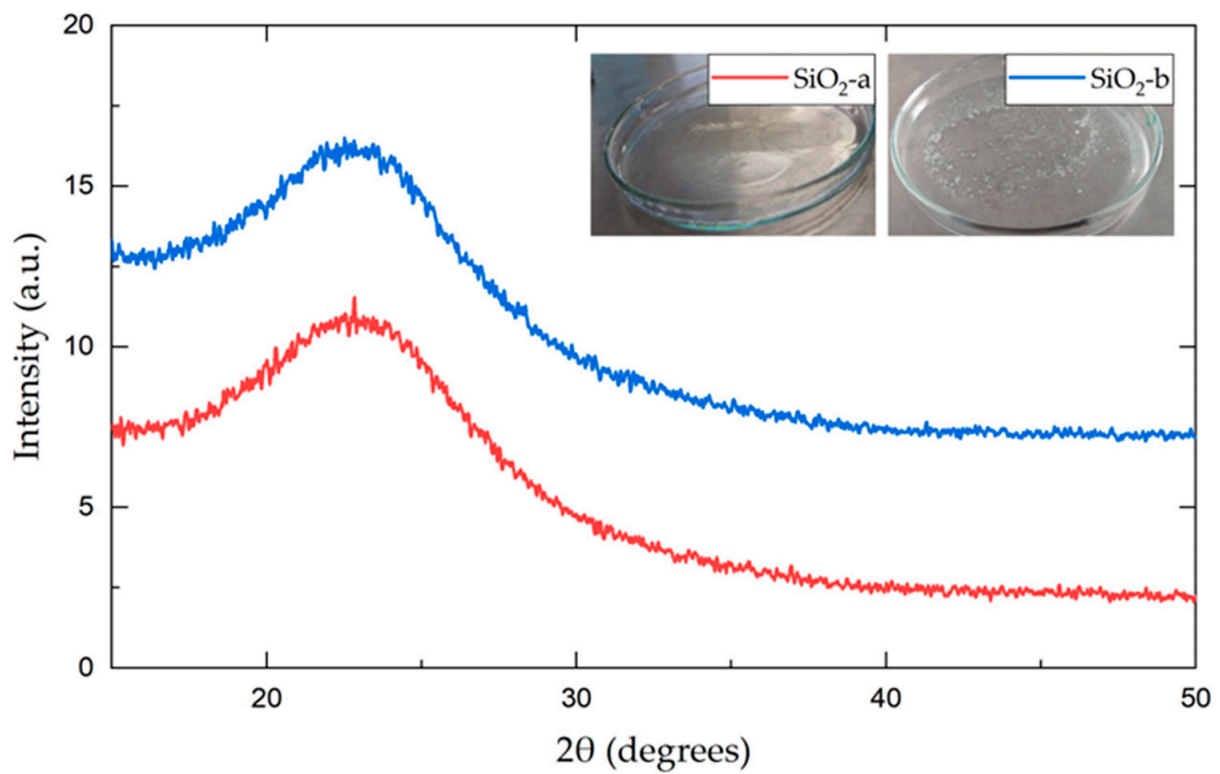
#### 3.1. SiO<sub>2</sub> NP Characterization

The inset in Figure 1a depicts images of the obtained gels for both syntheses: acid (SiO<sub>2</sub>-a) and alkaline (SiO<sub>2</sub>-b) catalysis. Upon comparing both systems, a clear qualitative distinction was observed. In the alkaline gel, clusters of whitish particles were noticed, while in the acid system, a homogeneous and transparent solid gel was formed. The whitish hue in the alkaline catalysis is commonly observed in spherical SiO<sub>2</sub> particles with particle sizes of around 100–150 nm [26]. In contrast, the transparent solution in the acidic catalysis could represent the formation of particles with dendritic structures with particles between 50 and 60 nm [27].

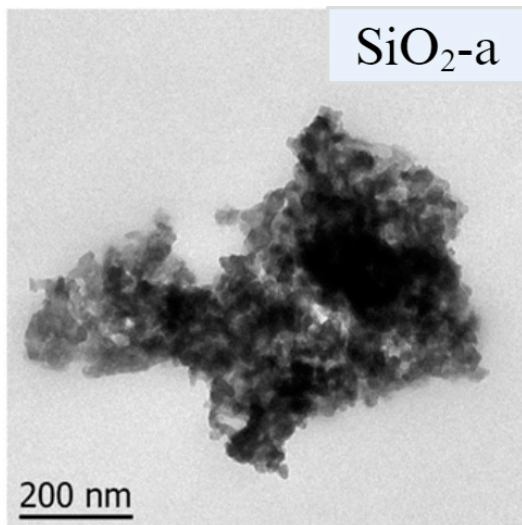
To determine the structural and morphological differences between the two synthesis processes, XRD and TEM techniques were performed from the synthesized SiO<sub>2</sub> particles in both alkaline and acidic media.

The diffractograms (see Figure 1a) show the typical broad signal generated by an amorphous material, corresponding to silica-based nanomaterials. This result is commonly observed in materials synthesized through the sol-gel process [29]. Both systems presented a wide Bragg reflection between 20° and 30°, with maximum intensities at 22.84° (SiO<sub>2</sub>-a) and 22.52° (SiO<sub>2</sub>-b). The TEM images of both the SiO<sub>2</sub>-a and SiO<sub>2</sub>-b particles (Figure 1b,c) show a high degree of agglomeration. However, there were significant differences in the particle size within the observed clusters. The SiO<sub>2</sub>-a particles, synthesized under acidic conditions, exhibited a smaller particle size and a lower agglomeration than those in SiO<sub>2</sub>-b, as previously reported [15].

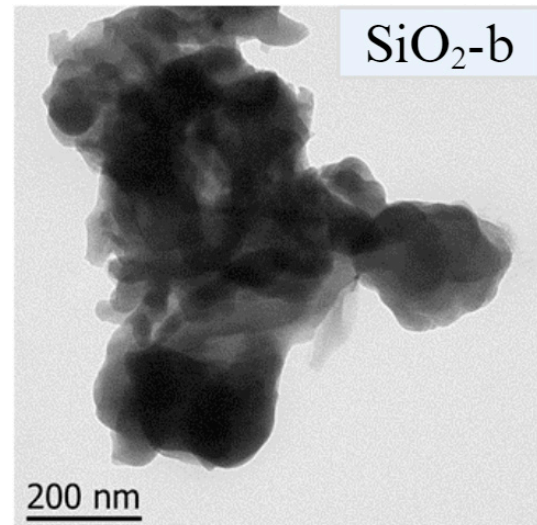
Figure 2a shows the Raman spectra obtained for SiO<sub>2</sub> particles. Six characteristic Raman-active vibrational modes were identified for both synthesis methods. R (380 cm<sup>-1</sup>) represents the flexion mode of oxygen atoms in Si-O-Si linkages, and D<sub>1</sub> (484 cm<sup>-1</sup>) corresponds to the “breathing” relaxation mode of 4-member rings. The mode at 802 cm<sup>-1</sup> is the vibration mode of the SiO<sub>2</sub> network optical branch, while the 876 cm<sup>-1</sup> is the contraction mode of Si-O-Si systems in the SiO<sub>2</sub> network. The signal at 976 cm<sup>-1</sup> corresponds to the vibration mode of the Si-OH molecule related to the surface silicon atoms. Finally, at 1041 cm<sup>-1</sup>, a stretching mode belonging to the Si-O-Si core bonds was observed [30]. The SiO<sub>2</sub>-a sample exhibited higher intensity in the six vibrational modes compared to the SiO<sub>2</sub>-b system. This may be attributed to a smaller particle size and a lower degree of agglomeration, as observed in the TEM images. This results in a larger surface area, which in turn leads to a stronger interaction with the Raman laser beam [31,32].



(a)



(b)



(c)

**Figure 1.** (a) X-ray diffractogram of sol-gel-synthesized SiO<sub>2</sub> particles under acidic (SiO<sub>2</sub>-a) and alkaline (SiO<sub>2</sub>-b) conditions. TEM images of acidic (b) and alkaline (c) SiO<sub>2</sub> nanoparticles.

In addition to the six characteristic Raman-active vibrational modes, two additional peaks were observed at  $1300\text{ cm}^{-1}$ . These peaks belong to both TEOS and alcohol molecules, such as ethanol [33]. Ethanol is one of the main by-products of the sol-gel condensation reaction used to synthesize the SiO<sub>2</sub> particles from TEOS [15]. The intensity of the alcohol-related peak was higher for the SiO<sub>2</sub>-b particles. This suggests that the SiO<sub>2</sub>-b particles contained a higher concentration of residual TEOS or ethanol.

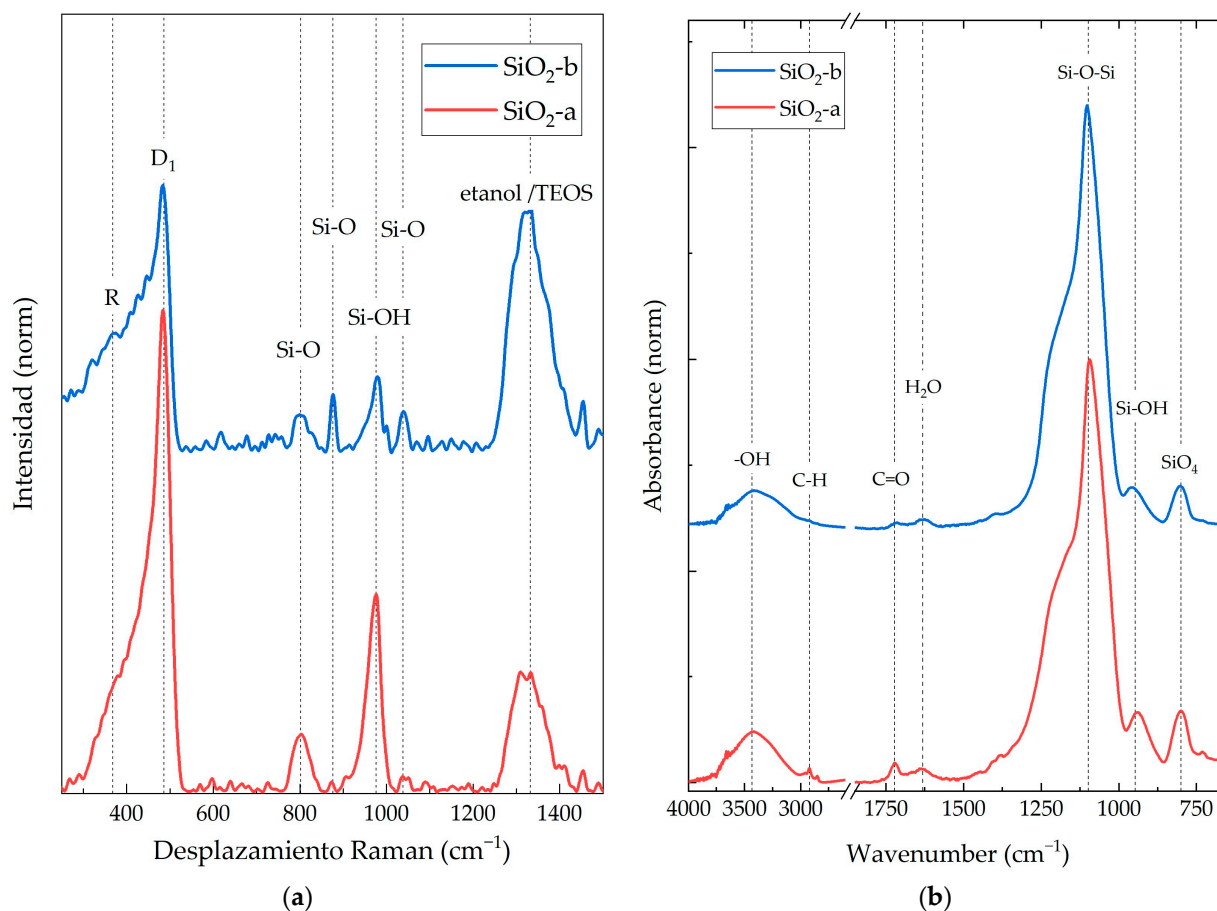


**Figure 2.** (a) Raman spectra and (b) FT-IR spectra of SiO<sub>2</sub> nanoparticles synthesized by the sol-gel method under acidic (SiO<sub>2</sub>-a) and alkaline (SiO<sub>2</sub>-b) conditions.

In Figure 2b, the FT-IR spectrum of the synthesized SiO<sub>2</sub> nanoparticles is presented. Both materials exhibited three characteristic vibrational modes of SiO<sub>2</sub> structures within the analyzed wavelength range: 800 cm<sup>-1</sup>, corresponding to the asymmetric stretching vibration of Si-O-Si; 1093–1250 cm<sup>-1</sup>, representing the symmetric stretching vibration of cyclic and linear silica molecules; and 940–959 cm<sup>-1</sup>, corresponding to Si-OH stretching vibrations modes [34].

The FT-IR spectrum reveals a wide vibrational mode around 3700–3000 cm<sup>-1</sup>, which is attributed to the stretching vibration of -OH groups. These hydroxyl groups are found on the surface of nanoparticles synthesized by sol-gel methods [15], as well as their TEOS precursors and by-products like ethanol or water. Additionally, vibrational modes in the regions of 1620–1650 cm<sup>-1</sup> and 1722–1750 cm<sup>-1</sup> were observed. These were attributed to adsorbed water molecules [34] and the stretching vibrations of carbonyl groups (C=O) from acetone [35], respectively. For both registered peaks, SiO<sub>2</sub>-a presented an intense absorbance peak of this functional group. Vibrational mode 2950–2850 cm<sup>-1</sup> corresponds to asymmetric stretching modes of C-H, which are characteristic of potential remnants of TEOS, ethanol, and acetone, as observed in Raman spectra [26].

Figure 3a shows the XPS survey spectra for both SiO<sub>2</sub> particulate systems (a and b), and Figure 3b shows the corresponding scans and deconvolution for C1s and Si2p species for the SiO<sub>2</sub>-b particles (the SiO<sub>2</sub>-a deconvolution process can be consulted in Figure S1). This spectrum allowed for the identification of the chemical species (Si, C, and O) as well as their functional groups (deconvolution), intensities, atomic percentages, and relationships between species. The obtained XPS results and deconvolution processes are listed in Table 1.

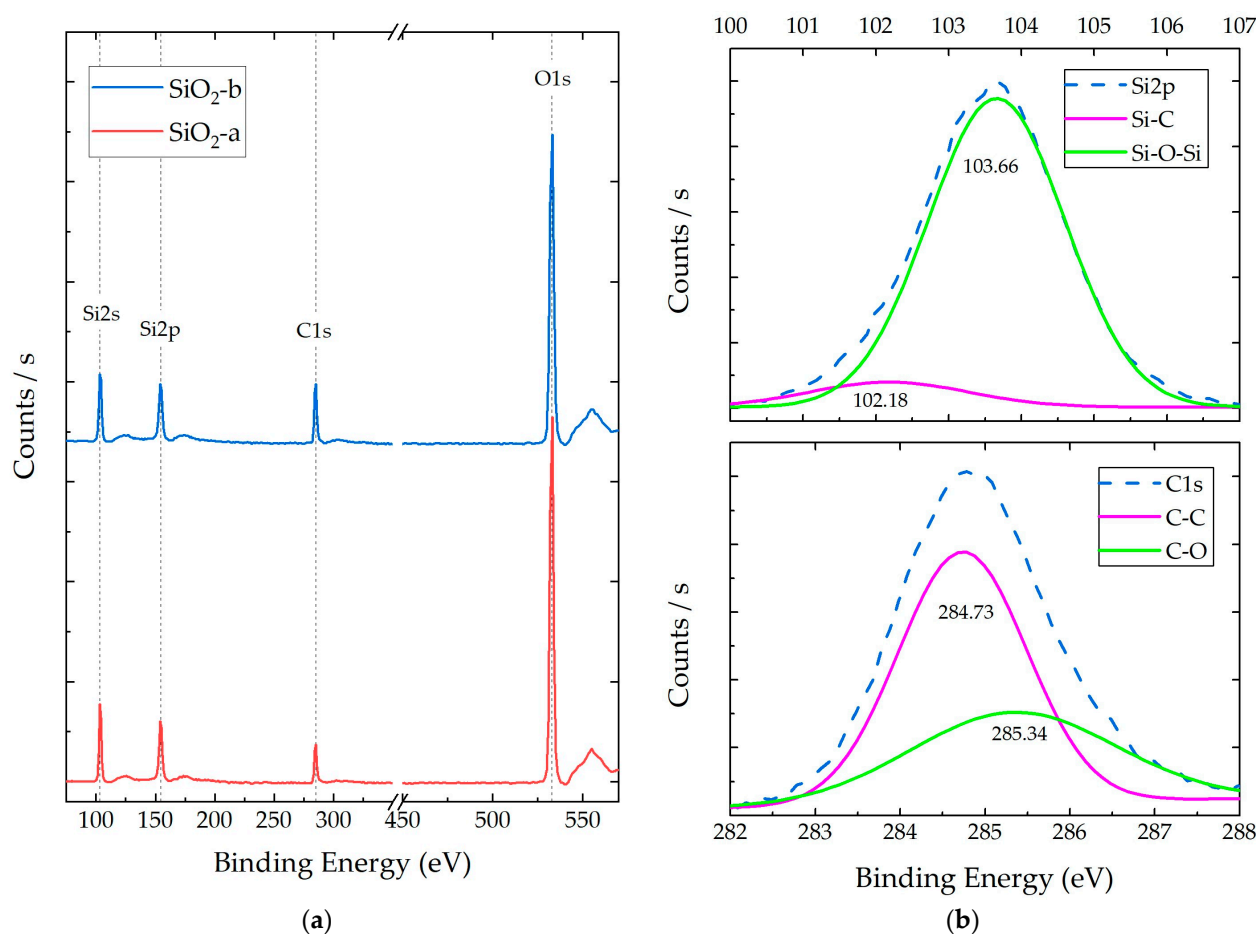


**Figure 3.** XPS spectra of synthesized SiO<sub>2</sub> particles under acidic (SiO<sub>2</sub>-a) and alkaline (SiO<sub>2</sub>-b) conditions: (a) survey spectra and (b) representative deconvolution analysis for Si2p and C1 orbitals of SiO<sub>2</sub>-b.

**Table 1.** XPS results of chemical species in synthesized SiO<sub>2</sub> (acid and alkaline) nanoparticles and deconvolution process for S2p and C1 orbitals.

	Species	Binding Energy (eV)	Intensity (CPS)	FWHM (eV)	Area (CPS•eV)	Area (Norm)	Atomic Conc. (%)	Atomic Ratio *
SiO <sub>2</sub> -a	Si2p	101.57	1359.45	1.06	1507.74	0.027	31.82%	1
		103.52	28,287.24	1.86	54,919.59	0.973		
	C1s	284.66	14,530.61	1.48	22,874.40	0.619	19.21%	0.6
		285.37	4922.10	2.68	14,052.02	0.381		
	O1s	532.85	135,607.75	1.71	259,798.74	1	48.97%	1.54
SiO <sub>2</sub> -b	Si2p	102.18	1919.39	2.54	5097.19	0.086	31.15%	1
		103.66	23,610.95	2.21	54,497.88	0.914		
	C1s	284.73	18,567.63	1.78	35,174.67	0.635	23.98%	0.76
		285.34	6675.72	2.84	20,190.43	0.365		
	O1s	532.93	111,300.88	2.08	256,032.04	1	44.87%	1.44

\* Atomic ratio between chemical species was calculated using the Si element as a calculus base.

In the XPS spectra, the presence of atomic orbitals belonging to Si and O was determined, both associated with the silica (SiO<sub>2</sub>) structure, as reported in [36]. These systems presented Si:O atomic ratios of 1:1.54 (SiO<sub>2</sub>-a) and 1:1.44 (SiO<sub>2</sub>-b). Additionally, the presence

of characteristic carbon orbitals (C1s) was observed, with a higher concentration in the SiO<sub>2</sub>-b samples. The evidence of these chemical species could correspond to precursors' remnants (acetone and TEOS) and by-products of hydrolysis and condensation reactions (ethanol) [37].

The XPS deconvolution analysis of the SiO<sub>2</sub> particles revealed the presence of two main peaks for the Si species, located at 101.57 and 103.52 eV for SiO<sub>2</sub>-a and at 102.18 and 103.66 for SiO<sub>2</sub>-b. These peaks can be attributed to the C-Si and Si-O-Si bonding configurations, respectively [38]. The C-Si bonds are present in the TEOS precursor, while the Si-O-Si bonds are characteristic of the SiO<sub>2</sub> network [36]. For the C species, two main peaks were also observed at 284.66 and 285.37 eV for SiO<sub>2</sub>-a and at 284.73 and 285.34 eV for SiO<sub>2</sub>-b. These peaks could be assigned to the C-C and C-O bonding configurations, respectively [39]. These species are present in both the TEOS precursor and the ethanol by-product.

### 3.2. PDMS-%SiO<sub>2</sub> Composite Chemical Characterization

#### 3.2.1. Composite Raman Spectroscopy

To identify the compositional differences between the synthesized composites, Raman, FT-IR, and XPS spectroscopies were performed. Figure 4a shows the Raman spectra of the PDMS 5:1-%SiO<sub>2</sub> composite group. This group had a weight ratio of 5:1 (PDMS:TEOS) and normalized intensities. The remaining 14 spectra of all study groups can be consulted in Figure S2. Table 2 summarizes the Raman-active vibrational modes identified in all composite materials; the relative intensity of neat PDMS; and the changes in the intensity ratios of the composites with SiO<sub>2</sub> nanoparticles (a and b) at concentrations of 5%, 10%, and 15%.

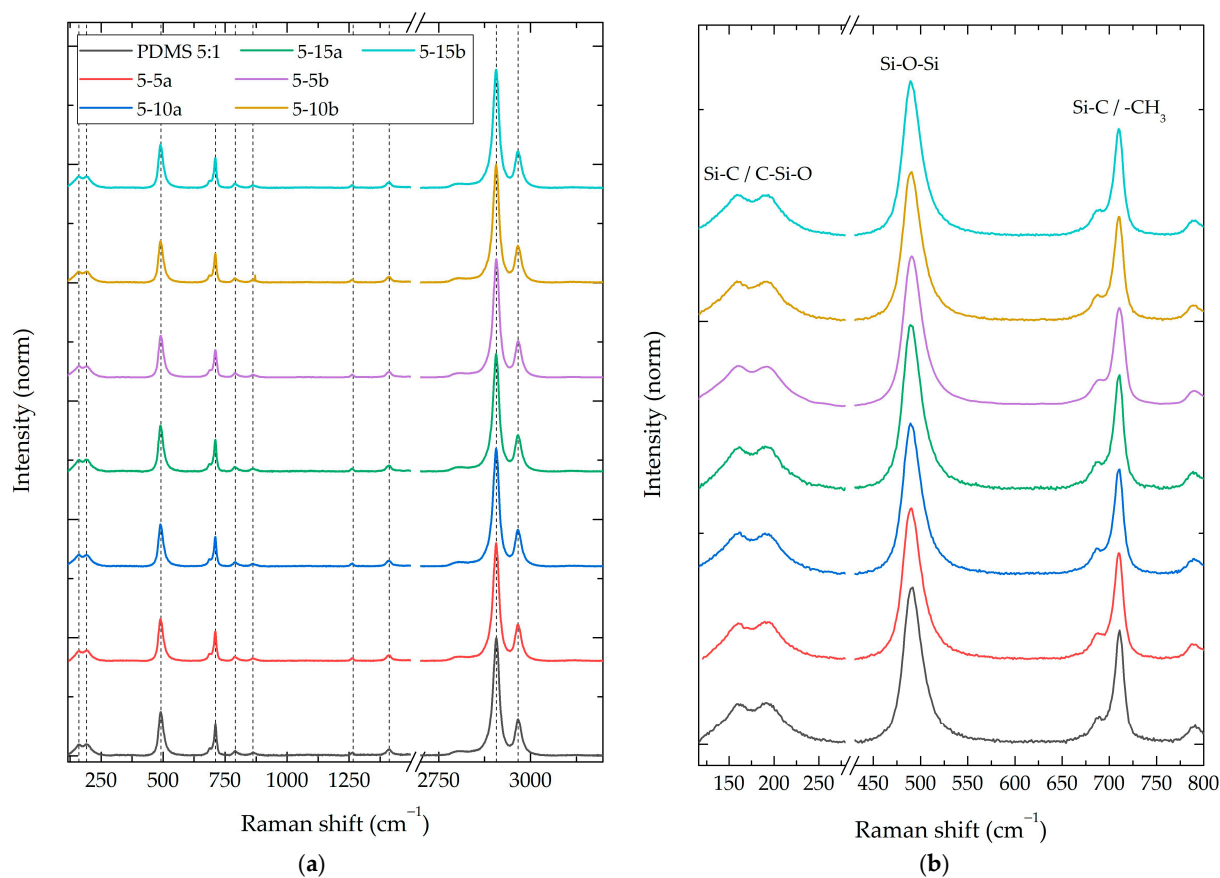


**Figure 4.** Raman spectra of PDMS 5:1 composite with different NPs SiO<sub>2</sub> concentrations (5%, 10%, and 15%). (a) Survey spectra and (b) 145–800 cm<sup>-1</sup> zoom in.

**Table 2.** Raman-active vibrational modes for crosslinked PDMS-%SiO<sub>2</sub> composites with Raman shift intensities varying by nanoparticle type and concentration [40].

PDMS 15:1									
Vibrational Mode [30]	Raman Shift (cm <sup>-1</sup> )	0% (Norm)	a			b			
			5%	10%	15%	5%	10%	15%	
1	Si-C torsion	157.40	0.075	1.66%	15.05%	22.79%	9.89%	11.56%	10.66%
2	C-Si-C deflection/C-Si-O deflection	192.63	0.078	5.22%	14.96%	24.07%	9.44%	11.54%	12.32%
3	Si-O-Si stretch	489.29	0.315	8.57%	12.73%	20.52%	10.85%	10.87%	10.18%
4	Si-C stretch	689.19	0.062	-6.23%	-0.55%	15.36%	-0.52%	-5.67%	-5.42%
5	Si-C symmetric stretch/CH <sub>3</sub> rock	709.69	0.232	-2.45%	0.52%	11.44%	-0.35%	-0.87%	-1.28%
6	Si-C stretch/CH <sub>3</sub> rock	788.66	0.038	-11.45%	-5.78%	16.30%	-8.77%	-14.81%	-7.58%
7	CH <sub>3</sub> asymmetric stretch	861.97	0.029	-19.45%	-24.79%	-3.16%	-26.19%	-30.09%	-33.75%
8	Si-CH <sub>3</sub> symmetric bending	1262.66	0.027	-18.41%	-18.05%	5.35%	-20.48%	-17.07%	-22.68%
9	CH <sub>3</sub> asymmetric bending	1410.73	0.05	-11.46%	-8.39%	2.10%	-6.95%	-4.50%	-4.90%
10	CH <sub>3</sub> symmetric stretch	2905.73	1	0.00%	0.00%	0.00%	0.00%	0.00%	0.00%
11	CH <sub>3</sub> asymmetric stretch	2965.55	0.309	1.02%	-0.27%	1.29%	0.86%	0.70%	2.21%
PDMS 10:1									
Vibrational Mode [30]	Raman Shift (cm <sup>-1</sup> )	0% (Norm)	a			b			
			5%	10%	15%	5%	10%	15%	
1	Si-C torsion	158.70	0.089	10.49%	3.61%	6.68%	-7.15%	-5.83%	-4.21%
2	C-Si-C deflection/C-Si-O deflection	192.63	0.092	4.82%	7.44%	2.78%	-5.11%	-3.93%	-3.82%
3	Si-O-Si stretch	490.54	0.36	0.85%	1.74%	2.15%	-5.51%	-2.98%	-4.54%
4	Si-C stretch	687.98	0.063	2.67%	1.84%	2.82%	-7.86%	-6.05%	-6.14%
5	Si-C symmetric stretch/CH <sub>3</sub> rock	710.89	0.252	0.12%	2.64%	-2.48%	-11.94%	-9.53%	-12.48%
6	Si-C stretch/CH <sub>3</sub> rock	791.04	0.035	7.32%	18.21%	10.76%	-7.61%	-0.43%	2.20%
7	CH <sub>3</sub> asymmetric stretch	864.32	0.025	0.81%	13.67%	3.35%	-8.93%	-9.13%	-4.39%
8	Si-CH <sub>3</sub> symmetric bending	1262.66	0.027	-5.66%	4.56%	-21.92%	-15.65%	-24.98%	-15.94%
9	CH <sub>3</sub> asymmetric bending	1412.88	0.05	-1.01%	5.61%	-5.93%	-5.47%	-7.43%	-3.61%
10	CH <sub>3</sub> symmetric stretch	2906.33	1	0.00%	0.00%	0.00%	0.00%	0.00%	0.00%
11	CH <sub>3</sub> asymmetric stretch	2965.55	0.311	-1.82%	-0.29%	-0.33%	-0.36%	0.49%	0.08%
PDMS 5:1									
Vibrational Mode [30]	Raman Shift (cm <sup>-1</sup> )	0% (Norm)	a			b			
			5%	10%	15%	5%	10%	15%	
1	Si-C torsion	160.01	0.097	-12.43%	4.69%	6.42%	-2.03%	-2.11%	1.69%
2	C-Si-C deflection/C-Si-O deflection	191.33	0.1	-10.55%	0.28%	4.83%	-6.90%	-5.89%	-0.85%
3	Si-O-Si stretch	491.78	0.373	-3.89%	-3.55%	4.92%	-5.31%	-5.55%	-1.36%
4	Si-C stretch	689.19	0.067	-4.59%	-4.90%	0.98%	-8.15%	-6.55%	-5.46%
5	Si-C symmetric stretch/CH <sub>3</sub> rock	710.89	0.271	-6.82%	-7.87%	1.02%	-16.78%	-9.40%	-6.32%
6	Si-C stretch/CH <sub>3</sub> rock	791.04	0.045	-18.12%	-13.81%	-0.22%	-24.81%	-18.59%	-16.84%
7	CH <sub>3</sub> asymmetric stretch	861.97	0.03	-19.22%	-18.80%	0.49%	-34.65%	-23.14%	-15.60%
8	Si-CH <sub>3</sub> symmetric bending	1265.97	0.03	-26.69%	-7.55%	-6.38%	-32.01%	-20.28%	-18.35%
9	CH <sub>3</sub> asymmetric bending	1411.80	0.058	-16.67%	-16.06%	-3.87%	-23.19%	-15.18%	-16.39%
10	CH <sub>3</sub> symmetric stretch	2907.15	1	0.00%	0.00%	0.00%	0.00%	0.00%	0.00%
11	CH <sub>3</sub> asymmetric stretch	2966.36	0.311	-0.43%	0.67%	0.54%	-1.04%	0.80%	-0.06%

For all synthesized composites, Raman-active vibrational modes of the PDMS polymer were identified [40], without the presence of new peaks or vibration energy (Raman shift) modifications. A modification in the relative intensities of the vibrational modes was observed between the different composite groups, showing a relative intensity reduction of 35% and increments up to 24% compared to the PDMS without particles.

The intensity results presented in Table 1 demonstrate a direct correlation between the weight ratio of PDMS:TEOS and the relative intensity of vibrational modes. The addition of SiO<sub>2</sub> particles at lower concentrations leads to a reduction in the relative intensities of the observed vibrational modes. As the particle concentration rises, an increase in relative intensity was observed in the 150–800 cm<sup>-1</sup> range (Figure 4b). This vibrational energy range aligns with the stronger characteristic Raman-active vibrational modes of the SiO<sub>2</sub> nanoparticle systems (Figure 2).

Additionally, the vibrational mode at  $2965\text{ cm}^{-1}$  also demonstrates a proportional increase in  $\text{SiO}_2$  concentration, suggesting the likely presence of residual TEOS/ethanol resulting from sol-gel reactions and crosslinking processes [26].

### 3.2.2. Composite Fourier-Transform Infrared Spectroscopy (FT-IR)

Figure 5 shows the FT-IR spectrum of the PDMS 5:1-% $\text{SiO}_2$  composite group. This group had a weight ratio of 5:1 (PDMS:TEOS) and normalized intensities. The remaining 14 FT-IR spectra of the study groups and PDMS, TEOS, and DBTDL reference spectra can be consulted in Figure S3. Table 3 displays the vibration wavelength of infrared-active characteristic bonds from crosslinked PDMS composites [41], along with their relative intensity and composites' intensity shifts because of  $\text{SiO}_2$  nanoparticles (a and b) at theoretical weight concentrations of 5%, 10%, and 15%.

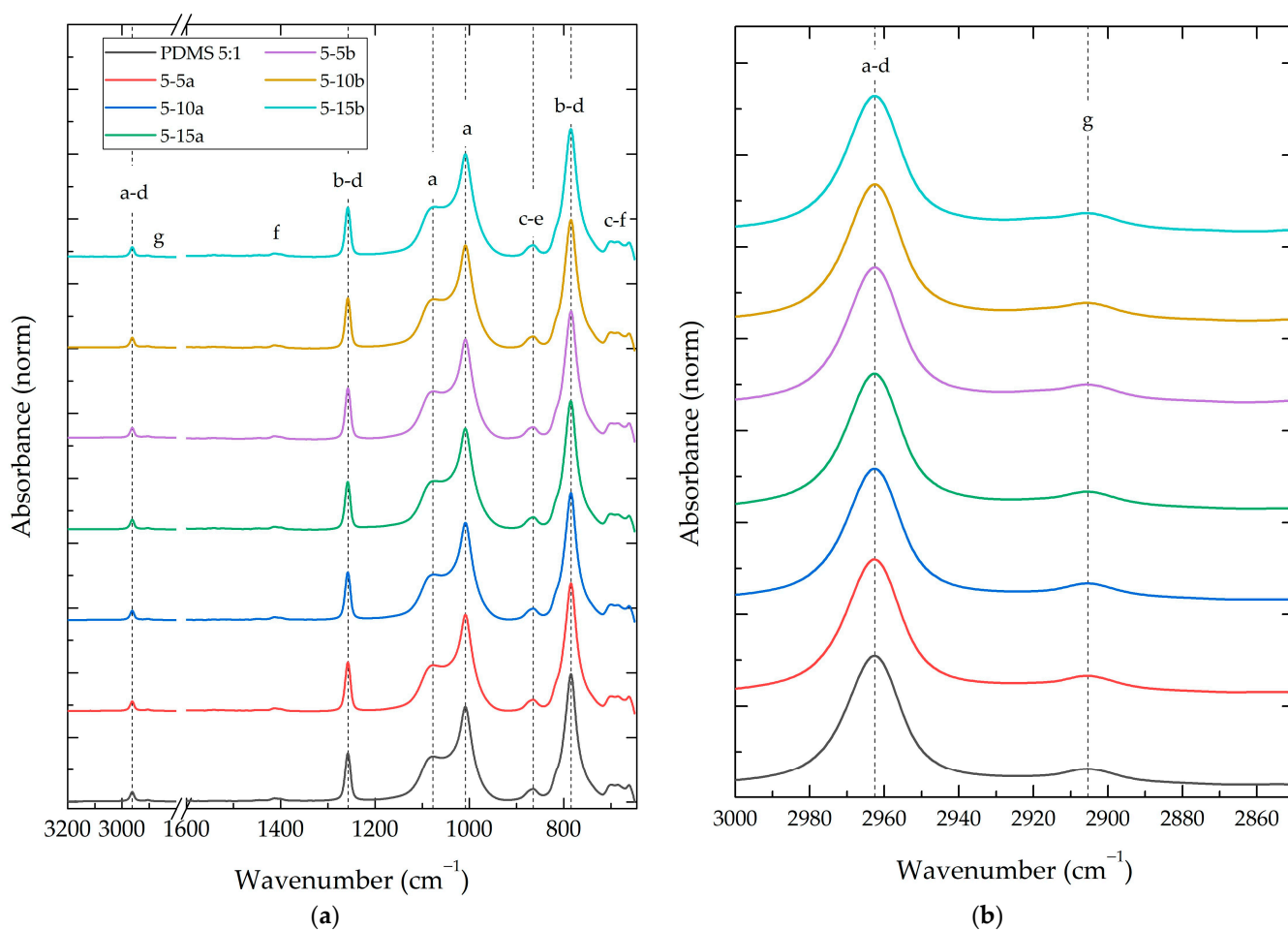


**Figure 5.** FT-IR spectra of PDMS 5:1 composite with different NP  $\text{SiO}_2$  types (a,b) and concentrations (5%, 10% and 15%). Letters a–g represent the observed vibration modes showed in Table 3.

An FT-IR analysis of the PDMS-% $\text{SiO}_2$  composites revealed minimal wavenumber shifts ( $<0.7\%$ ) in all identified vibrational modes compared to the neat PDMS:TEOS samples. This suggests a minimal influence of the  $\text{SiO}_2$  nanoparticles on the vibration energy of the polymer matrix, possibly due to a maintained similar chemical environment around the vibrating groups [10]. In contrast, the relative intensities of the vibrational modes in the composites exhibited significant changes compared to the neat PDMS:TEOS materials, ranging from  $-14\%$  to  $+59\%$  changes in relative intensities.

**Table 3.** FT-IR-active vibrational modes for crosslinked PDMS-%SiO<sub>2</sub> composites and relative intensity variation [41].

PDMS 15:1									
Wavenumber (cm <sup>-1</sup> )	Vibration Mode	0%	a			b			
			5%	10%	15%	5%	10%	15%	
f	660.5	Si-CH <sub>3</sub>	0.14	-5.97%	-13.31%	-15.51%	-6.13%	-7.39%	-3.58%
c	684.61	Si-(CH <sub>3</sub> ) <sub>3</sub>	0.14	-9.92%	-15.95%	-16.54%	-13.98%	-12.65%	-5.63%
c	699.55	Si-(CH <sub>3</sub> ) <sub>3</sub>	0.14	-9.39%	-14.22%	-14.77%	-14.40%	-13.11%	-4.44%
b-d	784.4	Si(CH <sub>3</sub> ) <sub>2</sub> -O-Si(CH <sub>3</sub> ) <sub>2</sub> -/Si-(CH <sub>3</sub> ) <sub>3</sub>	1	0.00%	0.00%	0.00%	0.00%	0.00%	0.00%
c-e	864.44	Si-(CH <sub>3</sub> ) <sub>3</sub> /Si-OH	0.1	-2.91%	-9.36%	-10.64%	-8.84%	-8.16%	-2.86%
a	1008.11	Si-(CH <sub>3</sub> ) <sub>n</sub>	0.76	2.33%	2.86%	4.52%	3.36%	5.09%	6.64%
a	1077.53	Si-(CH <sub>3</sub> ) <sub>n</sub>	0.35	5.84%	6.04%	9.21%	8.91%	8.90%	14.60%
b-d	1257.36	Si(CH <sub>3</sub> ) <sub>2</sub> -O-Si(CH <sub>3</sub> ) <sub>2</sub> -/Si-(CH <sub>3</sub> ) <sub>3</sub>	0.41	2.64%	1.42%	0.21%	5.77%	4.60%	0.03%
f	1412.12	Si-CH <sub>3</sub>	0.03	-11.68%	18.42%	-0.16%	-7.53%	-0.13%	-7.23%
g	2905.72	C-H	0.02	19.77%	19.94%	15.16%	21.14%	38.46%	26.67%
a,d	2962.61	Si(CH <sub>3</sub> ) <sub>n</sub> /Si-(CH <sub>3</sub> ) <sub>3</sub>	0.08	3.52%	2.91%	3.15%	7.21%	10.57%	6.78%
PDMS 10:1									
Wavenumber (cm <sup>-1</sup> )	Vibration Mode	0%	a			b			
			5%	10%	15%	5%	10%	15%	
f	660.5	Si-CH <sub>3</sub>	0.13	3.30%	-1.93%	-2.04%	14.20%	9.34%	0.18%
c	684.61	Si-(CH <sub>3</sub> ) <sub>3</sub>	0.13	-3.72%	-5.46%	-2.15%	4.32%	-0.76%	-3.27%
c	699.55	Si-(CH <sub>3</sub> ) <sub>3</sub>	0.13	-4.19%	-4.39%	-1.32%	2.21%	-1.33%	-3.40%
b-d	784.89	Si(CH <sub>3</sub> ) <sub>2</sub> -O-Si(CH <sub>3</sub> ) <sub>2</sub> -/Si-(CH <sub>3</sub> ) <sub>3</sub>	1	0.00%	0.00%	0.00%	0.00%	0.00%	0.00%
c-e	864.44	Si-(CH <sub>3</sub> ) <sub>3</sub> /Si-OH	0.1	-3.36%	-0.27%	-6.30%	3.40%	3.23%	-1.29%
a	1008.11	Si-(CH <sub>3</sub> ) <sub>n</sub>	0.81	-8.03%	-4.26%	-2.26%	-3.50%	0.60%	0.62%
a	1077.05	Si-(CH <sub>3</sub> ) <sub>n</sub>	0.37	-5.24%	-1.53%	-1.61%	5.56%	10.05%	10.24%
b-d	1257.36	Si(CH <sub>3</sub> ) <sub>2</sub> -O-Si(CH <sub>3</sub> ) <sub>2</sub> -/Si-(CH <sub>3</sub> ) <sub>3</sub>	0.43	-9.49%	-6.03%	-5.15%	1.88%	1.91%	0.67%
f	1412.6	Si-CH <sub>3</sub>	0.03	-12.53%	4.92%	1.33%	34.26%	11.54%	25.17%
g	2905.72	C-H	0.02	-10.22%	-5.54%	-1.88%	26.84%	49.80%	19.59%
a,d	2962.125	Si(CH <sub>3</sub> ) <sub>n</sub> /Si-(CH <sub>3</sub> ) <sub>3</sub>	0.08	-9.16%	-5.96%	-3.00%	5.50%	12.44%	5.35%
PDMS 5:1									
Wavenumber (cm <sup>-1</sup> )	Vibration Mode	0%	a			b			
			5%	10%	15%	5%	10%	15%	
f	660.5	Si-CH <sub>3</sub>	0.13	-8.61%	-10.32%	-14.05%	-1.20%	-8.64%	-7.90%
c	685.09	Si-(CH <sub>3</sub> ) <sub>3</sub>	0.13	-9.93%	-6.73%	-7.98%	-5.34%	-5.77%	-5.15%
c	699.55	Si-(CH <sub>3</sub> ) <sub>3</sub>	0.13	-9.22%	-4.16%	-5.11%	-5.03%	-4.01%	-4.00%
b-d	784.4	Si(CH <sub>3</sub> ) <sub>2</sub> -O-Si(CH <sub>3</sub> ) <sub>2</sub> -/Si-(CH <sub>3</sub> ) <sub>3</sub>	1	0.00%	0.00%	0.00%	0.00%	0.00%	0.00%
c-e	864.44	Si-(CH <sub>3</sub> ) <sub>3</sub> /Si-OH	0.1	-6.99%	-3.89%	0.87%	-4.18%	-4.98%	-1.71%
a	1008.11	Si-(CH <sub>3</sub> ) <sub>n</sub>	0.74	1.52%	2.59%	5.93%	4.57%	7.73%	8.11%
a	1077.05	Si-(CH <sub>3</sub> ) <sub>n</sub>	0.35	1.38%	0.99%	7.03%	4.53%	7.50%	10.79%
b-d	1257.36	Si(CH <sub>3</sub> ) <sub>2</sub> -O-Si(CH <sub>3</sub> ) <sub>2</sub> -/Si-(CH <sub>3</sub> ) <sub>3</sub>	0.4	0.16%	-1.37%	-1.94%	4.09%	2.58%	1.95%
f	1412.12	Si-CH <sub>3</sub>	0.03	-8.22%	1.21%	-9.22%	-13.18%	-10.33%	17.51%
g	2905.24	C-H	0.02	5.83%	8.11%	7.29%	59.76%	24.65%	17.05%
a,d	2962.61	Si(CH <sub>3</sub> ) <sub>n</sub> /Si-(CH <sub>3</sub> ) <sub>3</sub>	0.08	3.15%	2.38%	4.47%	14.40%	8.26%	5.90%

The relative intensity changes revealed a gradual increase in intensity in regions corresponding to vibrational modes characteristic of Si-O-Si bonds in SiO<sub>2</sub> nanoparticles (1300–900 cm<sup>-1</sup>) [33]. This increase in intensity was more pronounced with higher SiO<sub>2</sub> concentrations. Additionally, a significant increase in the intensity of vibrational modes was observed in the range of 3000 to 2900 cm<sup>-1</sup>. This increase could be attributed to an increase in the -OH groups present on the surface of the SiO<sub>2</sub> particles [15].

### 3.2.3. Composite X-ray Photoelectron Spectroscopy (XPS)

Figure 6a shows the XPS results of the PDMS 15:1-%SiO<sub>2</sub> composite group. PDMS 10:1 and PDMS 5:1 survey XPS spectra can be consulted in Figure S4. Figure 6b shows the representative deconvolution process performed on the Si and C species for each polymer composite for PDMS 15:1–10%SiO<sub>2</sub>-a. The deconvolution process of PDMS 15:1–10%SiO<sub>2</sub>-a and all other composites can be consulted in Figure S5 for C1s and in Figure S6 for S2p.

This process identified the functional groups interacting with the Si and C species, as well as their concentration ratios.

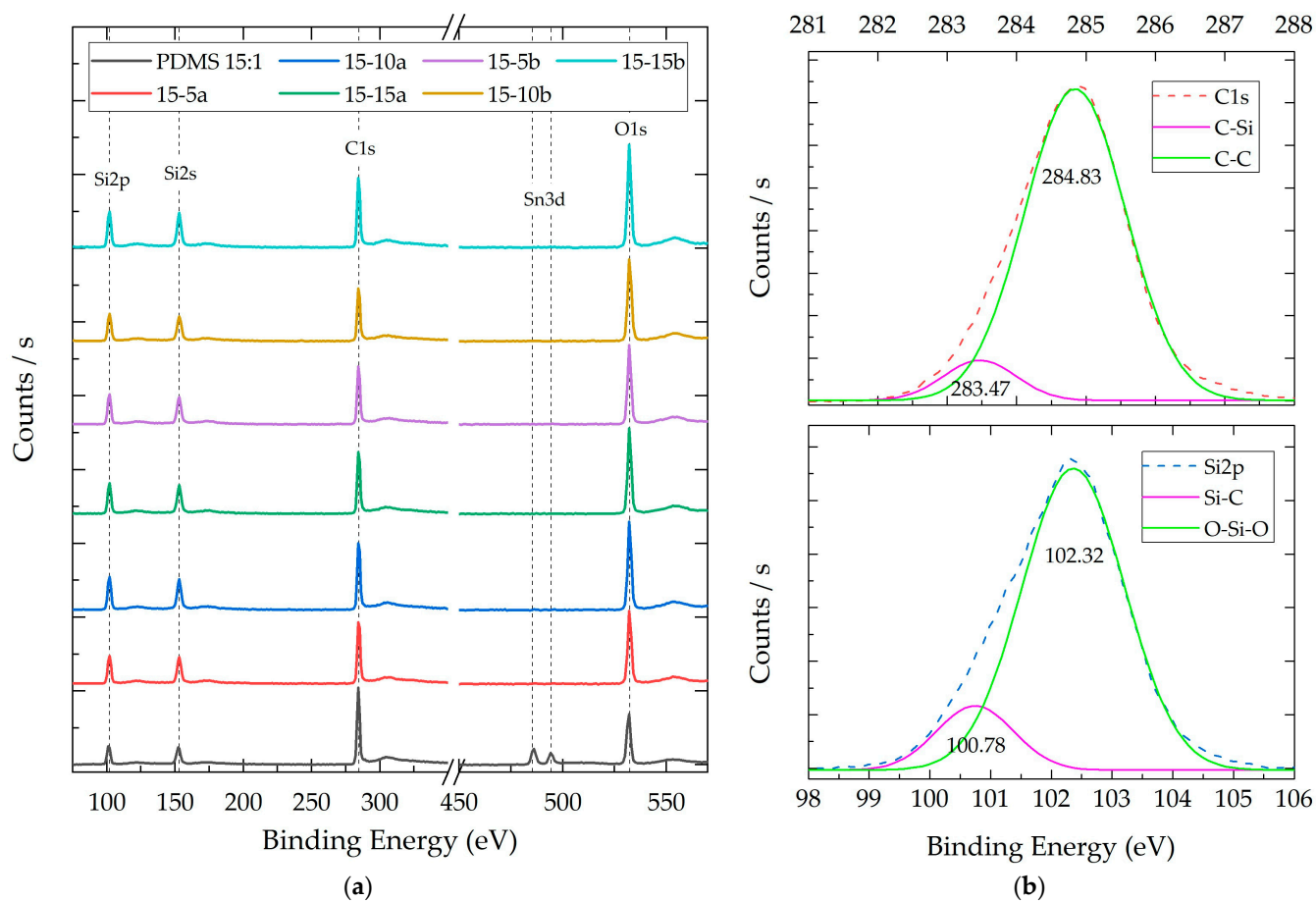


**Figure 6.** (a) Representative XPS survey spectra of composites with a 15:1 weight ratio (PDMS:TEOS) and different NP SiO<sub>2</sub> concentrations (5%, 10%, and 15%). (b) Representative deconvolution analysis for Si2p and C1 orbitals in PDMS 15:1–10% SiO<sub>2</sub>-a.

Table 4 shows the results obtained from the XPS analysis. This table shows the identified species (Si, C, and O); the signal intensity; the atomic percentage; and the atomic ratio between the atomic species of the composite materials.

Through the application of deconvolution processes to the polymeric composites, the presence of two components related to the Si species was discerned. Both components were identified in all composites and presented binding energy averages of  $100.68 \pm 0.13$  eV and  $102.30 \pm 0.08$  eV. These contributions are attributed to the Si-C and Si-O-Si bonds, respectively [38]. The Si-C bonds are commonly associated with methyl (CH<sub>3</sub>) functional groups, serving as substituents intricately linked to the primary chain of PDMS [42]. Conversely, the Si-O-Si bonds can be associated with the main chain groups of the PDMS structure, in addition to being integral to the core of the SiO<sub>2</sub> nanoparticles.

The deconvolution results for the carbon atom allowed for the identification of two components in all composite materials. These components presented binding energy averages of  $283.44 \pm 0.13$  eV and  $284.81 \pm 0.05$  eV and can be attributed to the C-Si and C-C species, respectively [42]. Unlike the SiO<sub>2</sub> nanoparticles, no components associated with C-O bonds, which typically manifest above 285 eV, were detected in these composites.

**Table 4.** XPS results of chemical species in PDMS-%SiO<sub>2</sub> composites and deconvolution process for Si and C species.

PDMS 15:1									
Species	Binding Energy (eV)	Intensity (CPS)	FWHM (eV)	Area (CPS•eV)	Area (Norm)	Atomic Conc. (%)	Atomic Ratio *	Relation Shift	
0%	Si2p	100.66	5009.84	1.54	8229.91	0.19	20.21%	1.000	-
		102.12	16,946.03	1.99	35,922.96	0.81			
	C1s	283.78	27,009.70	1.46	42,091.72	0.27	61.82%	3.059	-
		284.98	71,324.21	1.48	112,418.83	0.73			
		529.08	57,659.77	1.59	106,054.23	1.00			
O1s	482.38	13,153.65	2.07	50,075.61	1.00	0.91%	0.045	-	
5% a	Si2p	100.84	7870.52	1.60	13,418.41	0.22	25.54%	1.000	0.000
		102.30	25,513.39	1.80	48,861.13	0.78			
	C1s	283.39	10,737.10	1.21	13,828.33	0.09	53.62%	2.099	−0.959
		284.78	73,470.19	1.69	131,790.71	0.91			
O1s	526.00	82,874.91	1.62	152,715.54	1.00	20.84%	0.816	−0.028	
10% a	Si2p	100.78	7243.57	1.46	11,229.16	0.16	26.34%	1.000	0.000
		102.32	29,902.90	1.92	60,969.90	0.84			
	C1s	283.47	11,458.63	1.21	14,780.85	0.09	52.11%	1.978	−1.081
		284.83	78,640.31	1.71	143,052.16	0.91			
O1s	526.00	94,731.26	1.63	175,305.35	1.00	21.55%	0.818	−0.026	
15% a	Si2p	100.75	5996.81	1.49	9536.94	0.14	26.40%	1.000	0.000
		102.36	28,171.11	1.99	59,791.79	0.86			
	C1s	283.47	9441.53	1.23	12,359.82	0.08	51.30%	1.943	−1.116
		284.84	73,199.86	1.72	133,768.13	0.92			
O1s	526.00	91,951.90	1.63	170,697.23	1.00	22.30%	0.845	0.001	
5% b	Si2p	100.92	8986.55	1.54	14,696.63	0.22	27.37%	1.000	0.000
		102.40	26,703.67	1.81	51,393.55	0.78			
	C1s	283.45	11,868.31	1.36	17,127.24	0.13	50.46%	1.844	−1.215
		284.81	65,734.69	1.71	119,319.86	0.87			
O1s	526.08	86,589.05	1.60	158,313.86	1.00	22.17%	0.810	−0.034	
10% b	Si2p	100.54	3492.26	1.24	4616.74	0.08	26.08%	1.000	0.000
		102.31	24,503.38	2.17	56,610.91	0.92			
	C1s	283.48	10,530.95	1.17	13,088.25	0.10	50.40%	1.933	−1.126
		284.83	67,031.50	1.62	115,775.55	0.90			
O1s	526.00	85,752.56	1.66	163,780.62	1.00	23.52%	0.902	0.058	
15% b	Si2p	100.80	8372.29	1.53	13,591.69	0.17	27.19%	1.000	0.000
		102.38	33,761.94	1.88	67,485.20	0.83			
	C1s	283.48	15,322.67	1.20	19,562.28	0.12	49.84%	1.833	−1.226
		284.86	83,141.20	1.63	144,223.20	0.88			
O1s	526.08	109,943.27	1.61	203,118.13	1.00	22.98%	0.845	0.001	
PDMS 10:1									
Species	Binding Energy (eV)	Intensity (CPS)	FWHM (eV)	Area (CPS•eV)	Area (Norm)	Atomic conc. (%)	Atomic Ratio *	Relation Shift	
0%	Si2p	100.39	233.10	1.33	329.17	0.07	25.95%	1.000	-
		102.25	2147.49	1.93	4408.81	0.93			
	C1s	283.15	438.10	1.41	657.33	0.06	52.68%	2.030	-
		284.79	5821.64	1.67	10,319.33	0.94			
		532.37	6454.43	1.52	11,236.48	0.82			
O1s	532.37	6454.43	1.52	11,236.48	0.82	21.37%	0.824	-	

Table 4. Cont.

PDMS 10:1									
Species	Binding Energy (eV)	Intensity (CPS)	FWHM (eV)	Area (CPS•eV)	Area (Norm)	Atomic Conc. (%)	Atomic Ratio *	Relation Shift	
5% a	Si2p	100.68	5679.92	1.49	9038.24	0.15	25.62%	1.000	0.000
		102.30	25,206.02	1.84	49,283.79	0.85			
	C1s	283.35	9915.91	1.14	12,046.90	0.09			
		284.77	68,133.75	1.63	118,566.48	0.91			
O1s	532.40	80,913.78	1.60	148,934.83	0.87	22.19%	0.866	0.043	
10% a	Si2p	100.73	4663.48	1.43	7079.97	0.12	26.46%	1.000	0.000
		102.28	24,304.36	2.03	52,505.68	0.88			
	C1s	283.42	7865.35	1.19	9949.09	0.08			
		284.77	62,767.35	1.75	116,978.52	0.92			
O1s	532.42	82,356.19	1.57	148,456.83	0.84	22.33%	0.844	0.020	
15% a	Si2p	100.83	7234.27	1.49	11,474.71	0.18	25.78%	1.000	0.000
		102.35	25,715.67	1.87	51,260.25	0.82			
	C1s	283.51	12,468.89	1.26	16,769.45	0.12			
		284.84	71,719.00	1.68	128,095.72	0.88			
O1s	532.45	81,880.60	1.60	150,201.29	0.80	20.75%	0.805	−0.019	
5% b	Si2p	100.61	5895.03	1.42	8900.28	0.15	25.07%	1.000	0.000
		102.26	25,818.22	1.89	51,972.14	0.85			
	C1s	283.37	12,287.41	1.18	15,383.71	0.11			
		284.76	74,468.33	1.60	126,702.54	0.89			
O1s	532.36	85,026.62	1.63	158,707.76	0.87	21.83%	0.871	0.047	
10% b	Si2p	100.59	4233.19	1.32	5938.89	0.09	26.89%	1.000	0.000
		102.35	27,144.65	2.00	57,705.79	0.91			
	C1s	283.35	9908.59	1.15	12,088.14	0.09			
		284.77	67,028.12	1.62	115,583.89	0.91			
O1s	532.41	94,238.89	1.60	173,925.70	0.91	24.41%	0.908	0.084	
15% b	Si2p	100.51	2725.68	1.11	3232.76	0.05	27.17%	1.000	0.000
		102.43	26,596.30	2.20	62,273.85	0.95			
	C1s	283.44	8269.65	1.16	10,248.61	0.08			
		284.84	64,416.59	1.66	113,486.00	0.92			
O1s	532.54	99,166.24	1.67	188,714.81	0.97	26.22%	0.965	0.142	
PDMS 5:1									
Species	Binding Energy (eV)	Intensity (CPS)	FWHM (eV)	Area (CPS•eV)	Area (Norm)	Atomic conc. (%)	Atomic Ratio *	Relation Shift	
0%	Si2p	100.71	597.44	1.46	928.48	0.08	20.94%	1.000	-
		102.20	2736.10	2.07	6030.24	0.92			
	C1s	283.50	14,137.02	1.23	18,560.86	13.40			
		284.83	73,262.12	1.54	119,971.03	86.60			
		284.83	73,262.12	1.54	119,971.03	86.60			
O1s	532.37	8445.93	1.66	16,195.07	0.83	17.30%	0.826	-	
Sn3d	486.17	5100.06	2.08	19,964.75	1.16	24.30%	1.160	-	
5% a	Si2p	100.56	5524.30	1.42	8355.49	0.08	25.19%	1.000	0.000
		102.22	25,720.76	1.92	52,577.57	0.92			
	C1s	283.50	14,142.34	1.23	18,576.17	13.41			
		284.83	73,258.51	1.54	119,956.16	86.59			
O1s	532.41	84,872.40	1.62	158,280.22	0.88	22.06%	0.876	0.050	
10% a	Si2p	100.57	5524.30	1.42	8355.49	0.08	25.99%	1.000	0.000
		102.22	25,720.76	1.92	52,577.57	0.92			
	C1s	283.50	10,205.15	1.26	13,657.94	10.70			
		284.80	66,373.00	1.61	113,936.51	89.30			
O1s	532.50	87,513.28	1.61	161,871.71	0.90	23.41%	0.901	0.075	

Table 4. Cont.

		PDMS 5:1							
Species		Binding Energy (eV)	Intensity (CPS)	FWHM (eV)	Area (CPS•eV)	Area (Norm)	Atomic conc. (%)	Atomic Ratio *	Relation Shift
15% a	Si2p	100.73	918.92	1.49	1456.09	0.07	25.58%	1.000	0.000
		102.23	4952.13	2.03	10,696.51	0.93			
	C1s	283.46	1798.26	1.36	2596.39	9.56	51.86%	2.027	−0.806
		284.81	13,236.78	1.74	24,556.04	90.44			
O1s	532.52	16,964.46	1.59	31,657.35	0.88	22.55%	0.882	0.055	
5% b	Si2p	100.59	2754.67	1.23	3605.89	0.04	24.15%	1.000	0.000
		102.36	19,783.53	1.97	41,467.13	0.96			
	C1s	283.18	3733.70	0.96	3806.93	3.66	51.91%	2.149	−0.684
		284.80	53,565.28	1.76	100,322.67	96.34			
O1s	532.47	69,902.20	1.67	134,749.28	0.99	23.94%	0.991	0.165	
10% b	Si2p	100.86	6752.94	1.47	10,592.09	0.09	27.22%	1.000	0.000
		102.37	26,917.55	1.95	55,842.61	0.91			
	C1s	283.51	11,301.88	1.22	14,633.87	10.87	50.57%	1.858	−0.976
		284.85	65,557.64	1.72	120,000.53	89.13			
O1s	532.45	86,180.03	1.62	159,336.90	0.82	22.21%	0.816	−0.010	
15% b	Si2p	100.64	4419.27	1.32	6206.52	0.06	27.44%	1.000	0.000
		102.35	25,854.94	2.01	553,93.02	0.94			
	C1s	283.48	9092.33	1.18	11,413.69	9.84	48.15%	1.755	−1.079
		284.79	59,787.62	1.64	104,542.07	90.16			
O1s	532.45	88,917.78	1.60	163,418.89	0.89	24.41%	0.890	0.063	

\* Atomic ratio between chemical species was calculated using the Si element as a calculus base.

Through the atomic ratio comparison of the C/Si relation across the samples, it was observed that the PDMS:TEOS system with a lower degree of crosslinking (15:1) exhibits a higher carbon concentration with a 3.06 C/Si ratio. This ratio decreases for all other study groups, reaching a minimum of 1.74 in the PDMS5:1–10% b composite. Similarly, the atomic ratio of Si/O remains within the range of 0.82–0.84 for the polymers without SiO<sub>2</sub> particles. The composites with SiO<sub>2</sub> particles show an increase in the O/Si ratio, reaching up to 0.99.

#### 4. Discussion

Physicochemical analyses of silicon nanoparticles synthesized under acidic (SiO<sub>2</sub>-a) and alkaline (SiO<sub>2</sub>-b) conditions revealed distinct physical and chemical properties. Although both exhibited amorphous structures, as confirmed by XRD diffractograms (Figure 1a), macroscopic differences during gel-formation behaviors were observed. This suggests that the nanoparticles undergo distinct reaction pathways during the sol-gel process, which is influenced by the medium's pH, as previously reported [43].

As the sol-gel reactions advance, the functional groups bonded to the TEOS orthosilicate transform from ≡Si-O-Et to ≡Si-OH and ≡Si-O-Si≡, presenting a progressive decrease in electron density. In acidic media, H<sup>+</sup> ions preferentially react with species of a higher electron density (≡Si-O-Et), promoting hydrolysis and particle formation. Conversely, in an alkaline medium, OH<sup>−</sup> ions preferentially react with molecules of a lower electron density (≡Si-O-Si≡ or ≡Si-OH), favoring condensation and particle growth [15].

This expected behavior is consistent with the morphologies observed in the TEM images (Figure 1b,c). The SiO<sub>2</sub>-a particles exhibited smaller sizes and less agglomeration compared to the SiO<sub>2</sub>-b particles, which can be explained by the different reaction routes. In SiO<sub>2</sub>-a, promoting hydrolysis reactions prioritizes the formation of new particles with smaller sizes. In contrast, SiO<sub>2</sub>-b prioritizes particle growth due to the promotion of condensation, resulting in larger and more condensed particles [43].

The Raman, FT-IR, and XPS analyses confirmed that both the SiO<sub>2</sub>-a and SiO<sub>2</sub>-b particles possess similar chemical environments, containing the same chemical species, exhibiting similar vibrational energies, and displaying consistent O/Si atomic ratios (1.45 and 1.54, respectively). These results align with chemical properties encountered in silica sol-gel particles [30,33,36]. The presence of TEOS and ethanol molecules, common by-products in sol-gel processes, was confirmed by the identification of C-Si, C-O, C-C, and C-H species (Figure 6). A higher concentration of these species was observed in the SiO<sub>2</sub>-b particles, as evidenced by the stronger relative intensities in Raman and FT-IR spectra and a higher C1 atomic ratio in the XPS analysis (Table 4). Conversely, the SiO<sub>2</sub>-a particles presented a higher concentration of Si-OH species, which have been attributed to a greater hydroxylated surface area provoked by a smaller particle size for sol-gel particles without thermal treatments [15]. These results agree with the morphological differences between both particle systems.

Variations in species concentration between the two particle types are crucial as they will coexist with PDMS during in situ synthesis. Unlike previous studies where sol-gel by-products were eliminated through thermal treatments or filtration for chemical characterization [29], this analysis required the identification of all present species to identify those that will not be removed during the in situ process.

The Raman and FT-IR spectroscopy results of PDMS-%SiO<sub>2</sub> composites revealed no new vibrational modes and only minor modifications (less than 1%) in the wavenumber or Raman shift of the PDMS's bonds. This confirmed that the crosslinking density reached in these materials and the presence of particles did not alter the vibrational energy of the crosslinked PDMS, similar to observations for ex situ-synthesized PDMS-SiO<sub>2</sub> composites [29]. This behavior can be attributed to the structural similarities between the nanoparticles and PDMS (Si-O and Si-OH bonds), with TEOS undergoing a chemical process analogous to nanoparticle formation during crosslinking [11].

While no new vibrational modes were observed, changes in the relative intensities of the composites' spectra were identified compared to the PDMS:TEOS neat materials (15:1, 10:1, and 5:1). When the concentration of the crosslinking agent increased, the relative intensity of the PDMS vibrational modes remained constant or exhibited a slight increase. Conversely, in the presence of SiO<sub>2</sub> particles, the composites displayed an initial decrease in the relative intensity of the vibrational modes in both the Raman and FT-IR spectra (−35% and −14%, respectively). This phenomenon has been previously reported and attributed to modifications in the polymer's electron density because of the particle–polymer interaction [44]. The inherent competition between reactions during an in situ sol-gel synthesis can potentially alter the PDMS:TEOS ratio [3].

An increase in particle concentration within the composites resulted in a corresponding rise in the intensity ratio of specific spectral regions. In the Raman spectra, this enhancement was observed between 150 and 700 cm<sup>−1</sup>, while in the FT-IR spectra, it ranged from 900 to 1400 cm<sup>−1</sup>. A literature review and characterization results of SiO<sub>2</sub> nanoparticles revealed that these spectral regions agree with the characteristic vibrational modes of SiO<sub>2</sub>. For the Raman spectra, the R and D<sub>1</sub> vibrational modes (300–500 cm<sup>−1</sup>) corresponded to the “breathing” relaxation mode of Si-O rings [30]. Similarly, in the FT-IR spectra, the observed increase falls within the range of the asymmetric stretching mode of SiO<sub>4</sub> core structures (1300–1000 cm<sup>−1</sup>) [33]. This has been related to the fact that an increase in the concentration of a particular species within a system could lead to corresponding alterations in the spectral regions associated with its characteristic vibrational modes, resulting in intensified or decreased peaks for the neat material [45].

The XPS analysis corroborated the presence of Si, O, and C in all the composites, aligning with the expected elements for silicon polymers [42]. Silicon and oxygen constitute the main chain of polysiloxane, while carbon corresponds to the methyl groups (−CH<sub>3</sub>) bonded to silicon atoms along the polymer chain. Trace amounts of tin (Sn<sup>3d</sup>) were also detected in the XPS spectra, exhibiting variations in intensity without a discernible pattern

across the composites. The presence of these traces can be attributed to the DBTDL catalyst employed in the polymer crosslinking reaction [46].

While the same species were identified, their relative atomic proportions differed significantly between the composites. Notably, a reduction in the C/Si atomic ratio was observed with increasing SiO<sub>2</sub> particle concentrations. This trend suggests that the decrease is not due to a lower abundance of carbon species but rather an increase in Si and O originating from the sol-gel particles. This hypothesis is further supported by the increasing C1 signal area in the composites compared to PDMS, which represents a more atomic concentration for the XPS technique [10].

Deconvolution revealed the absence of C-O species, suggesting a clear distinction from the synthesized SiO<sub>2</sub> particles. This implies that no detectable remnants of precursors or by-products, such as TEOS or ethanol, are present on the XPS analysis surface [47]. These species might have been consumed during the polymer crosslinking reactions, as previous studies have demonstrated the feasibility of PDMS:crosslinker ratios up to 2:1 [48].

The O/Si ratio (0.82–0.99) displayed a slight increase with the particle concentration, yet it did not reach the values typically observed in SiO<sub>2</sub> nanoparticles (1.54). This lines up with the O/Si ratios commonly reported for PDMS:TEOS structures [41]. This behavior can potentially be attributed to the presence of nanoparticles within the nanocomposite, as an increase in the concentration of SiO<sub>2</sub> species likely originates an increase in Si and O species intensity [10].

The results indicate that composites with a higher particle concentration (PDMS-15%a and PDMS-15%b) exhibit a greater increase in the relative intensity of characteristic PDMS vibrational modes within the aforementioned spectral regions. Additionally, the composite PDMS-15%b displayed the most significant reduction in the Si/C ratio compared to all PDMS:TEOS investigated ratios (15:1, 10:1, and 5:1). These findings successfully confirm the presence and differentiation of SiO<sub>2</sub> particles within the composite system compared to the response of PDMS with different crosslinker relations, as explored in previous studies [48].

## 5. Conclusions

This study investigated the in situ synthesis of PDMS-SiO<sub>2</sub> nanoparticle composites, evaluating the influence of various parameters on their properties. These parameters included the crosslinking degree, particle concentration, and the type of sol-gel catalyst (acidic or alkaline).

Physicochemical analyses revealed distinct morphologies and surface chemistries for SiO<sub>2</sub> nanoparticles prepared under acidic and alkaline conditions (SiO<sub>2</sub>-a and SiO<sub>2</sub>-b). These differences were attributed to the impact of pH on the reaction pathways during the sol-gel process. Notably, the analyses highlighted the importance of synthesis conditions in defining the final properties of the SiO<sub>2</sub> particles, particularly regarding particle size, agglomeration, and the presence of by-products (TEOS and ethanol). This information provides valuable insights into how these factors might influence the interaction with PDMS during an in situ synthesis.

Raman, FT-IR, and XPS analyses confirmed the successful incorporation of SiO<sub>2</sub> nanoparticles into the PDMS matrix without altering the PDMS's chemical structure. However, the presence of nanoparticles did affect the relative intensities of specific vibrational modes, suggesting an interaction between the polymer and particles (variations from −35% to +24% for Raman and from −14% to +59% for FT-IR). Furthermore, the concentration of SiO<sub>2</sub> particles significantly impacted the XPS results. Composites with higher particle concentrations (PDMS-15%SiO<sub>2</sub>-a and PDMS-15%SiO<sub>2</sub>-b) exhibited the maximum decrease in the C/Si ratio (minimum 1.715) and the higher increase in the intensity of SiO<sub>2</sub> characteristic spectral regions (with a maximum O/Si ratio of 0.99), confirming the presence and modification response to different reticulation degrees and SiO<sub>2</sub> concentrations.

These findings demonstrate the feasibility of the proposed in situ sol-gel method for synthesizing PDMS-SiO<sub>2</sub> composites with tunable properties. By controlling synthesis parameters, researchers can tailor the final characteristics of the composites. This study

lays the groundwork for the further exploration of the relationship between synthesis conditions and the resulting composite properties of this novel synthesis method.

Once the successful synthesis of these in situ nanocomposites is obtained, future research should focus on a more in-depth analysis of the reaction kinetics and the nature of the nanoparticle–polymer interaction. This deeper understanding will facilitate the optimization of properties like mechanical response, thermal resistance, hydrophobicity, etc. Ultimately, such advancements will bridge the gap between “one-step” synthesis methods and their integration into broader polymer production processes at both research and industrial scales.

**Supplementary Materials:** The following supporting information can be downloaded at: <https://www.mdpi.com/article/10.3390/polym16081125/s1>. Figure S1: Deconvolution analysis for Si2p and C1 orbitals of SiO<sub>2</sub>-a particles. Figure S2: Raman spectra of (a) PDMS 15:1-%SiO<sub>2</sub> and (b) PDMS 10:1-%SiO<sub>2</sub> composites. Figure S3: FT-IR spectra of (a) PDMS 15:1-%SiO<sub>2</sub> and (b) PDMS 10:1-%SiO<sub>2</sub> composites. Figure S4: XPS spectra of (a) PDMS 10:1-%SiO<sub>2</sub> and (b) PDMS 5:1-%SiO<sub>2</sub> composites. Figure S5: Deconvolution analysis for C1 species of PDMS-%SiO<sub>2</sub> composites: C1s (dash), C-Si (magenta), and C-C (green). Figure S6: Deconvolution analysis for Si2p species of PDMS-%SiO<sub>2</sub> composites: Si2p (dash), Si-C (magenta), and O-Si-O (green).

**Author Contributions:** Conceptualization, A.C., R.V.-C. and K.E.; methodology, A.C.; validation, J.V.C.-R., R.V.-C. and K.E.; formal analysis, A.C., J.V.C.-R., R.F.V.-C. and K.E.; investigation, A.C.; resources, J.V.C.-R. and K.E.; data curation, A.C., R.F.V.-C. and K.E.; writing—original draft preparation, A.C.; writing—review and editing, A.C., J.V.C.-R., R.V.-C. and K.E.; supervision, J.V.C.-R., R.V.-C. and K.E.; project administration, K.E. All authors have read and agreed to the published version of the manuscript.

**Funding:** J.V.C.-R. acknowledges support from CONAHCyT Projects 1360 and 248378.

**Institutional Review Board Statement:** No applicable.

**Informed Consent Statement:** No applicable.

**Data Availability Statement:** Data are contained within the article.

**Acknowledgments:** A. Cordoba thanks CONAHCyT for a granted scholarship. The TEM images were carried out by Lourdes Palma Tirado at Instituto de Neurobiología, UNAM. The XPS analyses were carried out by Wilian Javier Cauich at Laboratorio Nacional de Nano y Biomateriales, Cinvestav-IPN. This research was funded by the FOMIX-Yucatán 2008-108160 and CONAHCyT LAB-2009-01-123913, 292692, 294643, 188345, and 204822 projects. The XRD analyses were carried out at the National Laboratory of Nano and Biomaterials, Cinvestav-IPN. This research was funded by the FOMIX-Yucatán 2008-108160 and CONAHCyT LAB-2009-01-123913, 292692, 294643, 188345, and 204822 projects. Special thanks go to Patricia Quintana for providing access to LANNBIO, to Daniel Aguilar Treviño for obtaining the diffractograms, and to Mario Herrera for the corrective maintenance of the D-8 Advance diffractometer.

**Conflicts of Interest:** The authors declare no conflicts of interest.

## References

1. PS Market Research. *Polymer Market Research Report*; Prescient & Strategic Intelligence: Delhi, India, 2022.
2. Madidi, F.; Momen, G.; Farzaneh, M. Dielectric Properties of TiO<sub>2</sub>/Silicone Rubber Micro- and Nanocomposites. *Adv. Mater. Sci. Eng.* **2018**, *2018*, 4682076. [[CrossRef](#)]
3. Fu, S.; Sun, Z.; Huang, P.; Li, Y.; Hu, N. Nano Materials Science Some Basic Aspects of Polymer Nanocomposites: A Critical Review. *Nano Mater. Sci.* **2019**, *1*, 2–30. [[CrossRef](#)]
4. Ali AlMaadeed, M.; Carignano, D.P.; Carignano, M.A. Polymer Science and Innovative Applications. In *Polymer Science and Innovative Applications*; Elsevier: Amsterdam, The Netherlands, 2020; pp. i–iii, ISBN 9780128168080.
5. Eduok, U.; Faye, O.; Szpunar, J. Recent Developments and Applications of Protective Silicone Coatings: A Review of PDMS Functional Materials. *Prog. Org. Coat.* **2017**, *111*, 124–163. [[CrossRef](#)]
6. Aly, K.; Aboubakr, S.H.; Bradford, P.D. One-step Fabrication of Bulk Nanocomposites Reinforced by Carbon Nanotube Array Fragments. *Polym. Compos.* **2022**, *43*, 94–110. [[CrossRef](#)]

7. Li, J.; Liu, H.; Guo, J.; Hu, Z.; Wang, Z.; Wang, B.; Liu, L.; Huang, Y.; Guo, Z. Flexible, Conductive, Porous, Fibrillar Polymer-Gold Nanocomposites with Enhanced Electromagnetic Interference Shielding and Mechanical Properties. *J. Mater. Chem. C* **2017**, *5*, 1095–1105. [[CrossRef](#)]
8. Chungprempree, J.; Preechawong, J.; Nithitanakul, M. Developing an Effective and Durable Film for Marine Fouling Prevention from PDMS/SiO<sub>2</sub> and PDMS/PU with SiO<sub>2</sub> Composites. *Polymers* **2022**, *14*, 4252. [[CrossRef](#)] [[PubMed](#)]
9. Cui, X.; Zhu, G.; Pan, Y.; Shao, Q.; Zhao, C.; Dong, M.; Zhang, Y.; Guo, Z. Polydimethylsiloxane-Titania Nanocomposite Coating: Fabrication and Corrosion Resistance. *Polymer* **2018**, *138*, 203–210. [[CrossRef](#)]
10. Krishna, D.N.G.; Philip, J. Review on Surface-Characterization Applications of X-Ray Photoelectron Spectroscopy (XPS): Recent Developments and Challenges. *Appl. Surf. Sci. Adv.* **2022**, *12*, 100332. [[CrossRef](#)]
11. Gupta, N.S.; Lee, K.; Labouriau, A. Tuning Thermal and Mechanical Properties of Polydimethylsiloxane with Carbon Fibers. *Polymers* **2021**, *13*, 1141. [[CrossRef](#)]
12. Zhang, F.; Yang, R.; Lu, D. Investigation of Polymer Aging Mechanisms Using Molecular Simulations: A Review. *Polymers* **2023**, *15*, 1928. [[CrossRef](#)]
13. Zhang, X.; Liu, F.; Xu, L.; Xu, Z.; Shen, C.; Zhang, G.; Meng, Q.; Gao, C. Heterostructured ZIF-8/Lamellar Talc Composites Incorporated Polydimethylsiloxane Membrane with Enhanced Separation Performance for Butanol Recovery. *J. Membr. Sci.* **2022**, *650*, 120433. [[CrossRef](#)]
14. Ashraf, M.A.; Peng, W.; Zare, Y.; Rhee, K.Y. Effects of Size and Aggregation/Agglomeration of Nanoparticles on the Interfacial/Interphase Properties and Tensile Strength of Polymer Nanocomposites. *Nanoscale Res. Lett.* **2018**, *13*, 214. [[CrossRef](#)] [[PubMed](#)]
15. Levy, D.; Zayat, M. *The Sol-Gel Handbook: Synthesis, Characterization, and Applications*; Wiley-VCH: Weinheim, Germany, 2015.
16. Chen, G.; Dai, Z.; Ding, S.; Lei, M.; Lin, J.; Wang, S.; Zhou, Y.; Pan, H.; Zhou, B. Realization of Integrative Hierarchy by In-Situ Solidification of ‘Semi-Cured’ Microcilia Array in Candle Flame for Robust and Flexible Superhydrophobicity. *Chem. Eng. J.* **2022**, *432*, 134400. [[CrossRef](#)]
17. Pandey, K.; Bindra, H.S.; Paul, D.; Nayak, R. Smart Multi-Tasking PDMS Nanocomposite Sponges for Microbial and Oil Contamination Removal from Water. *J. Polym. Res.* **2020**, *27*, 189. [[CrossRef](#)]
18. Wang, Q.; Che, J.; Wu, W.; Hu, Z.; Liu, X.; Ren, T.; Chen, Y.; Zhang, J. Contributing Factors of Dielectric Properties for Polymer Matrix Composites. *Polymers* **2023**, *15*, 590. [[CrossRef](#)] [[PubMed](#)]
19. Ríos, E.A.; Vega-Baudrit, J.R.; Villegas, J.G.; Sánchez, J.A. Silicon Nanostructures in Biomedicine and Biotechnology. *Momento* **2020**, *60*, 18–40. [[CrossRef](#)]
20. Harito, C.; Bavykin, D.V.; Yulianto, B.; Dipojono, H.K.; Walsh, F.C. Polymer Nanocomposites Having a High Filler Content: Synthesis, Structures, Properties, and Applications. *Nanoscale* **2019**, *11*, 4653–4682. [[CrossRef](#)] [[PubMed](#)]
21. Chen, C.; Xue, Y.; Li, Z.; Wen, Y.; Li, X.; Wu, F.; Li, X.; Shi, D.; Xue, Z.; Xie, X. Construction of 3D Boron Nitride Nanosheets/Silver Networks in Epoxy-Based Composites with High Thermal Conductivity via in-Situ Sintering of Silver Nanoparticles. *Chem. Eng. J.* **2019**, *369*, 1150–1160. [[CrossRef](#)]
22. Yuan, T.; Cui, X.; Liu, X.; Qu, X.; Sun, J. Highly Tough, Stretchable, Self-Healing, and Recyclable Hydrogels Reinforced by in Situ-Formed Polyelectrolyte Complex Nanoparticles. *Macromolecules* **2019**, *52*, 3141–3149. [[CrossRef](#)]
23. Santiago-Castillo, K.; Del Angel-López, D.; Torres-Huerta, A.M.; Domínguez-Crespo, M.A.; Palma-Ramírez, D.; Willcock, H.; Brachetti-Sibaja, S.B. Effect on the Processability, Structure and Mechanical Properties of Highly Dispersed in Situ ZnO:CS Nanoparticles into PVA Electrospun Fibers. *J. Mater. Res. Technol.* **2021**, *11*, 929–945. [[CrossRef](#)]
24. Bathini, S.; Raju, D.; Badilescu, S.; Packirisamy, M. Effect of Cross-Linking and Thermal Budget on Plasmonic Sensing and Sub-Surface Segregation of in Situ Synthesized Gold in Polymer Nanocomposite. *J. Nanoparticle Res.* **2021**, *23*, 21. [[CrossRef](#)]
25. Yorseng, K.; Siengchin, S.; Ashok, B.; Rajulu, A.V. Nanocomposite Egg Shell Powder with in Situ Generated Silver Nanoparticles Using Inherent Collagen as Reducing Agent. *J. Bioresour. Bioprod.* **2020**, *5*, 101–107. [[CrossRef](#)]
26. Lazareva, S.V.; Shikina, N.V.; Tatarova, L.E.; Ismagilov, Z.R. Synthesis of High-Purity Silica Nanoparticles by Sol-Gel Method. *Eurasian Chem. J.* **2017**, *19*, 295–302. [[CrossRef](#)]
27. Bhatt, N.; Mishra, A.; Goswami, R.; Prasad, B. Preparation of Silica Nano-Particles by Sol-Gel Method and Its Characterization. *J. Graph. Era Univ.* **2021**, *9*, 215–230. [[CrossRef](#)]
28. Rosales, A.; Maury-Ramírez, A.; Mejía-De Gutiérrez, R.; Guzmán, C.; Esquivel, K. SiO<sub>2</sub>@TiO<sub>2</sub> Coating: Synthesis, Physical Characterization and Photocatalytic Evaluation. *Coatings* **2018**, *8*, 120. [[CrossRef](#)]
29. Cordoba, A.; Rivera-Muñoz, E.M.; Velázquez-Castillo, R.; Esquivel, K. PDMS/TiO<sub>2</sub> and PDMS/SiO<sub>2</sub> Nanocomposites: Mechanical Properties’ Evaluation for Improved Insulating Coatings. *Nanomaterials* **2023**, *13*, 1699. [[CrossRef](#)] [[PubMed](#)]
30. Aguiar, H.; Serra, J.; González, P.; León, B. Structural Study of Sol-Gel Silicate Glasses by IR and Raman Spectroscopies. *J. Non-Cryst. Solids* **2009**, *355*, 475–480. [[CrossRef](#)]
31. Hoffmann, G.G. *Infrared and Raman Spectroscopy*; De Gruyter: Berlin, Germany, 2023; ISBN 9783110717556/9783110717549.
32. Alessi, A.; Agnello, S.; Buscarino, G.; Gelardi, F.M. Raman and IR Investigation of Silica Nanoparticles Structure. *J. Non-Cryst. Solids* **2013**, *362*, 20–24. [[CrossRef](#)]
33. Rubio, F.; Rubio, J.; Oteo, J.L. A FT-IR Study of the Hydrolysis of Tetraethylorthosilicate (TEOS). *Spectrosc. Lett.* **1998**, *31*, 199–219. [[CrossRef](#)]

34. Lu, Y.-K.; Yan, X.-P. An Imprinted Organic–Inorganic Hybrid Sorbent for Selective Separation of Cadmium from Aqueous Solution. *Anal. Chem.* **2004**, *76*, 453–457. [[CrossRef](#)]
35. Hudson, R.L.; Gerakines, P.A.; Ferrante, R.F. IR Spectra and Properties of Solid Acetone, an Interstellar and Cometary Molecule. *Spectrochim. Acta Part A Mol. Biomol. Spectrosc.* **2018**, *193*, 33–39. [[CrossRef](#)] [[PubMed](#)]
36. Roy, T.; Wanchoo, S.K.; Pal, K. Synergetic Proton-Conducting Effect of Sulfonated PEEK-MO<sub>2</sub>-CNT Membranes for PEMFC Applications. *Ionics* **2021**, *27*, 4859–4873. [[CrossRef](#)]
37. Schubert, U. Part One Sol–Gel Chemistry and Methods. *Sol-Gel Handb. Synth. Charact. Appl.* **2015**, 1–28. [[CrossRef](#)]
38. Ferrara, M.C.; Mirengi, L.; Mevoli, A.; Tapfer, L. Synthesis and Characterization of Sol–Gel Silica Films Doped with Size-Selected Gold Nanoparticles. *Nanotechnology* **2008**, *19*, 365706. [[CrossRef](#)] [[PubMed](#)]
39. Moulder, J.F.; Strickle, W.F.; Sobol, P.E. *Handbook of X-ray Photoelectron Spectroscopy*, 1st ed.; Perkin-Elmer Corporation: Eden Prairie, MN, USA, 1992.
40. Bistričić, L.; Borjanović, V.; Mikac, L.; Dananić, V. Vibrational Spectroscopic Study of Poly(Dimethylsiloxane)-ZnO Nanocomposites. *Vib. Spectrosc.* **2013**, *68*, 1–10. [[CrossRef](#)]
41. Mark, J.E. *Polymer Data Book*, 1st ed.; University of Cincinnati: Cincinnati, OH, USA, 1999.
42. Hong, H.; Zhang, J.; Zhu, Y.; Tse, S.D.; Guo, H.; Lai, Y.; Xi, Y.; He, L.; Zhu, Z.; Yin, K.; et al. In Situ Polymer-Solution-Processed Graphene–PDMS Nanocomposites for Application in Intracranial Pressure Sensors. *Nanomaterials* **2024**, *14*, 399. [[CrossRef](#)] [[PubMed](#)]
43. Dhahir, M.; Khyoon, H. Study the Effect of PH Variation on the Particle Size of SiO<sub>2</sub> Thin Films. *Iraqi J. Laser* **2016**, *15*, 1–8.
44. Atta, A.; Abdeltwab, E. Influence of Ion Irradiation on the Surface Properties of Silver-Coated Flexible PDMS Polymeric Films. *Braz. J. Phys.* **2022**, *52*, 3. [[CrossRef](#)]
45. Melvin, G.J.H.; Ni, Q.-Q.; Suzuki, Y.; Natsuki, T. Microwave-Absorbing Properties of Silver Nanoparticle/Carbon Nanotube Hybrid Nanocomposites. *J. Mater. Sci.* **2014**, *49*, 5199–5207. [[CrossRef](#)]
46. Hoflund, G.B.; Gonzalez, R.I.; Phillips, S.H. In Situ Oxygen Atom Erosion Study of a Polyhedral Oligomeric Silsesquioxane-Polyurethane Copolymer. *J. Adhes. Sci. Technol.* **2001**, *15*, 1199–1211. [[CrossRef](#)]
47. Post, P.; Wurlitzer, L.; Maus-Friedrichs, W.; Weber, A. Characterization and Applications of Nanoparticles Modified In-Flight with Silica or Silica-Organic Coatings. *Nanomaterials* **2018**, *8*, 530. [[CrossRef](#)] [[PubMed](#)]
48. Seghir, R.; Arscott, S. Extended PDMS Stiffness Range for Flexible Systems. *Sens. Actuators A Phys.* **2015**, *230*, 33–39. [[CrossRef](#)]

**Disclaimer/Publisher’s Note:** The statements, opinions and data contained in all publications are solely those of the individual author(s) and contributor(s) and not of MDPI and/or the editor(s). MDPI and/or the editor(s) disclaim responsibility for any injury to people or property resulting from any ideas, methods, instructions or products referred to in the content.